Role of Multi-Walled Carbon Nanotube Addition in Superconducting Properties of $Bi_2Sr_2CaCu_2O_{8+s}$ Glass–Ceramic Superconductors

K. Yakinci* and Ö. Çiçek

Department of Basic Engineering Sciences, Faculty of Engineering and Natural Sciences, Iskenderun Technical University, 31200, Iskenderun/Hatay, Turkey

Received: 13.06.2022 & Accepted: 17.11.2022

Doi: 10.12693/APhysPolA.143.298 *e-mail: kubra.yakinci@yahoo.com

In this work, pure and with 1, 3, 5, 10, and 15 wt% multi-walled carbon nanotube addition $Bi_2Sr_2CaCu_2O_{8+s}$ glass–ceramic materials have been investigated in terms of thermal, structural, microstructural, electrical, and magnetic properties. Multi-walled carbon nanotubes with a purity of 96% were used to enhance electrical transport properties. Thermal properties have been examined using differential thermal analysis. According to the differential thermal analysis, the multi-walled carbon nanotube addition reduced the melting temperature and slightly increased the crystallization activation energy of the BiSrCaCuO material. X-ray analyses showed that all samples have tetragonal symmetry and did not change with addition, but a small change in the c-axis is observed. Scanning electron microscope analyses showed no significant morphological change. The effect of the additive on the resistivity measurements was found to be limited, and zero resistance temperature increased up to a level of 5 wt% addition and then decreased drastically for higher addition cases. The hole concentration of the samples was calculated, and it was found that there was a shift towards the over-doped region with the addition. For the transport critical current density measurements, the highest increase of about 30% was obtained for the sample with 5 wt% multi-walled carbon nanotube addition, but in high addition cases, significant losses were obtained. A similar situation occurred in magnetization versus magnetic field measurements, and the highest magnetization critical current density value obtained ẅas 4.1×10^6 A/cm^2 at 4.2 K in the 5 wt% multi-wall carbon nanotube added sample.

topics: multi-wall carbon nanotube, high-temperature superconductors, BSCCO glass–ceramic, BSCCO superconductors

1. Introduction

Many new superconductor systems have been discovered over the past 30 years, some of which have been thoroughly studied and found to be insufficient for technological applications, but some of them were found important in terms of their properties and technological applications. The BiSrCaCuO (BSCCO) superconductor family is one of them, and scientific and technological studies are still being carried out on it [1]. The BSCCO materials can be easily prepared with several different production methods, and forms such as bulk, thin/thick film, cable, and ribbon can be easily made. In addition, its toxicity is lower than that of other high-temperature superconductors (HTS), such as Hg- or Tl-based systems. Considering the high critical current density (J_c) reaching $\sim 10^5$–10^6 A/cm^2 [2], and especially the high upper critical field (H_{c2}), the BSCCO material is technologically useful and applicable [3].

In principle, in HTS materials, high J_c values are required for technological applications. But J_c is limited by the weak intergranular connections or formation of impurity phases at the atomic scale at the grain boundaries due to the granular structure of these materials. Therefore, to increase J_c, the connection between the grains needs to be improved. The anisotropy, particularly in the H_{c2} and J_c characteristics of HTS materials, is also an important matter. Recently, it was found that the preferential orientation of grains and good texturing can reduce anisotropy by strengthening intergranular connections, causing a significant increase in J_c and H_{c2} of the HTS materials [4, 5].

Up to now, various attempts to improve BSCCO HTS materials have been made, such as using different production methods, including single-crystal fabrications and well-known solid-state preparation methods [6–9]. Besides these, the glass–ceramic method can also show significant results if the final heat treatment is performed in a controlled manner [10–12]. In addition, the creation of artificial defects by substitution or doping of magnetic or non-magnetic oxides and ion irradiation, as a columnar defect, is another known suitable methods to attempt to increase particularly the J_c's of thin/thick films [13–17].

Together with this, the layered structure, as well as the weakly coupled peculiarity of BSCCO samples, enable substitution, doping, and/or addition of various elements [18–29]. However, according to recent literature, the doping and/or substitution effect did not give a positive result except for a few oxide compounds such as PbO, SbO, and AgO, which act as flux agents in the structure and reduce the impurity phase formation, especially at the grain boundaries. The scattering effect appeared to be important due to the imbalances in the carrier concentration level, which caused negative results on both T_c and J_c [30–33]. Theoretically, this situation is explained by the research groups by the pair-breaking mechanism [34]. In addition, doping/substitution instead of the copper site gives more drastic results, especially if a magnetic ion is added. This situation can be explained by a change in vacancy position (for oxygen), electronic limitation, and band filling, as explained in earlier works [35, 36].

In the literature, it is seen that detailed studies on the carbon nanotube (CNT) or multi-wall carbon nanotube (MWCNT) doping/substitution, particularly for the BSCCO HTS system, are limited. At the same time, it is thought that CNT and/or MWCNTs, in nano size with cylindrical structure, are some of the candidates that can increase J_c of BSCCO superconductors by improving the flux pinning ability if added in an appropriate ratio with suitable preparation method.

Recently, Galvan et al. [37] showed experimental evidence of a minor improvement in J_c by irradiation-generated CNT intercalation in BSCCO polycrystalline samples. Other studies have shown that since, from a geometric point of view, carbon nanotubes have a comparable form and dimension to the columnar defects induced in BSCCO by irradiation, it will be possible to improve the intergranular critical current density if CNTs and/or MWCNTs can be embedded into a BSCCO matrix properly [37–41]. However, these studies also found that the reaction between oxygen and carbon is important, and in most cases, it emerges as a significant problem for the concordance of the results. It was also stated by many researchers that the wetting of CNTs by the BSCCO structure, to improve the flux pinning mechanism is an important issue [38–41]. In this context, the aim was to add various concentrations of MWCNTs to $Bi_2Sr_2CaCu_2O_{8+s}$ superconductors to improve their electrical transport properties, especially for J_c peculiarity, and the samples were prepared for the first time in the literature by the conventional glass–ceramic route.

2. Experimental methods

For the preparation of glass–ceramic MWCNT-added superconducting $Bi_2Sr_2CaCu_2O_{8+s}$ materials, high purity (Sigma-Aldrich, 99.5%) Bi_2O_3, $SrCO_3$, $CaCO_3$, and CuO oxide powder materials were used. After weighing the raw materials in the appropriate ratio to obtain $Bi_2Sr_2CaCu_2O_{8+s}$ nominal composition, they were mixed for 60 min. Then, the raw material was calcined twice in the Al_2O_3 pot at 750 and 810°C for 24 h.

Multi-walled carbon nanotubes, with an outer diameter of < 2 nm and inner diameter of < 1 nm, having 96% purity and 2.4 g/cm^3 bulk density (Nanografi), were added to the raw material with the ratio of 1, 3, 5, 10, and 15 wt% and mixed for 60 min at room temperature. Then raw material was placed into an Al_2O_3 pot and sintered in an argon environment at 775°C for 24 h. The mixed material was grained and heated in an argon environment at 985°C for 100 min for melting. The reason for using an argon atmosphere during the processes is to prevent destructive reactions of MWCNT with BSCCO material. We know from previous experience that BSCCO melts in an argon atmosphere at lower temperatures than in the air, completely melting at 970°C instead of at about 1100°C. Accordingly, in this study, the maximum temperature of 985°C was chosen for melting, and after 100 min, completely melted material was obtained. The melted material was then removed from the furnace and poured onto a 1 cm thick copper plate to obtain a glass phase.

The obtained glass pieces of different sizes were then heated at 840°C for 120 h in an oxygen gas atmosphere with 10°C/min heating/cooling ramps to convert them into the glass–ceramic form.

First, the differential thermal analysis (DTA) was performed to analyze samples to understand whether MWCNT affects the crystallization of $Bi_2Sr_2CaCu_2O_{8+s}$ material or not. Analyses were performed between 30°C and 1000°C at a heating rate of 5, 10, 20, and 30°C/min with non-sintered glass samples using the PerkinElmer DTA system and α-Al_2O_3 reference powder with platinum crucibles. The crystallization activation energies were then calculated using the Kissinger method.

X-ray diffraction (XRD) technique and pole figure analysis were performed for crystal structure and texture analysis. Analyses were done on the Malvern Panalytical EMPYREAN XRD system in the range of $2\theta = 3$–$80°$ using a Cu K_α ($\lambda = 1.5405$ Å) radiation.

Compositional and morphological analyses were performed at 20 kV using Thermo Fisher Scientific (FEI) Apreo S LoVac Scanning Electron Microscope (SEM) and Thermo Scientific UltraDry energy dispersive X-ray detector (EDS).

The zero-field cooling (ZFC) procedure was applied for electrical, magnetization, and I–V measurements. At the heating stage, different fields, parallel to the sample surface, were systematically applied in the range of ±8 T, and data were collected. Measurements were carried out with the Quantum Design PPMS-9 T and vibrating sample magnetometer (VSM) attachment. We used rectangular bar-shaped samples with dimensions of $6 \times 4 \times 2$ mm^3 for electrical and magnetic

TABLE I

The DTA data and calculated E_a and Avrami parameters of glass samples at a different heating rate.

MWCNT addition [wt%]	T_g [°C]	T_{cr1} [°C]	$T_{\mathrm{endo.}}$ [°C]	$T_{\mathrm{par.melt.}}$ [°C]	E_a [kJ/mol]	Avrami parameter n
Heating rate $\alpha = 5$°C/min						
0.0	430	496	840	885	331	2.11
1	430	495	840	886	332	2.11
3	429	493	842	887	336	2.12
5	428	489	844	888	340	2.18
10	426	487	848	890	344	2.23
15	424	485	850	895	350	2.25
Heating rate $\alpha = 10$°C/min						
0.0	431	497	841	886	331	2.14
1	431	496	841	886	332	2.14
3	430	494	842	887	336	2.15
5	427	491	843	889	341	2.21
10	425	489	849	891	345	2.24
15	422	486	851	897	351	2.26
Heating rate $\alpha = 20$°C/min						
0.0	437	503	847	893	333	2.17
1	436	502	847	894	335	2.18
3	435	499	848	897	338	2.19
5	432	497	849	899	344	2.25
10	430	494	855	902	349	2.28
15	428	491	858	908	355	2.31
Heating rate $\alpha = 30$°C/min						
0.0	444	510	853	904	336	2.19
1	442	508	854	906	339	2.19
3	440	505	856	909	342	2.20
5	437	503	857	914	347	2.26
10	434	500	861	918	352	2.35
15	431	498	866	921	359	2.39

measurements. We also used rectangular bar-shaped samples with a dimension of $1 \times 0.65 \times 0.25$ mm^3 for I–V measurements. For transport critical current calculations (J_c^{tran}), the cross-sectional area of the samples and the 1 μV criterion were taken into account.

3. Results and discussions

3.1. DTA analysis

In Fig. 1, the DTA results of glass samples, obtained with a 10°C/min heating rate, are given as an example. It has been observed that different levels of MWCNT addition show no significant change in the crystallization peculiarity of glass samples and that all of the samples produced had a similar exothermic and/or endothermic trend, with the exception of an increase in the thermal activity temperatures, i.e., samples that shifted to higher temperatures slightly changed compared to the pure BSCCO (see Fig. 1 and Table I). In general, a small endothermic activity appeared between 422°C and 444°C, depending on the heating ramp, before the first exotherm, representing the glass transition (T_g). Then the first crystallization temperatures (T_{cr1}), obtained between 485 and 510°C, and the second exothermic activity (T_{cr2}), obtained between 525 and 553°C, indicated crystallization of metastable phases, e.g., the formation of CaO, CuO, or Ca_2CuO_3 phases. The third exothermic activity (T_{cr3}) obtained between 775 and 810°C is believed to be due to crystallization or phase transformation into the first ($B_2Sr_2CuO_{6+y}$) and/or second ($Bi_2Sr_2CaCu_2O_{8+y}$) members of the BSCCO superconductor family. The endothermic dips that started to appear at around 840°C were evaluated to be due to partial melting, and the second dip, obtained at over 870°C, is believed to be due to the complete melting of the samples. These results reveal that all produced samples have initially been in the glass phase and then converted into the glass–ceramic form by applying an appropriate heat treatment cycle.

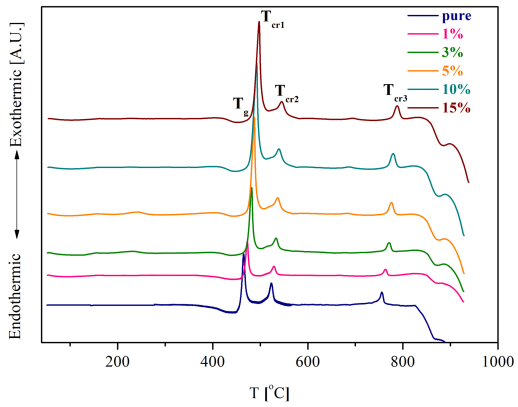

Fig. 1. DTA curves of the samples prepared.

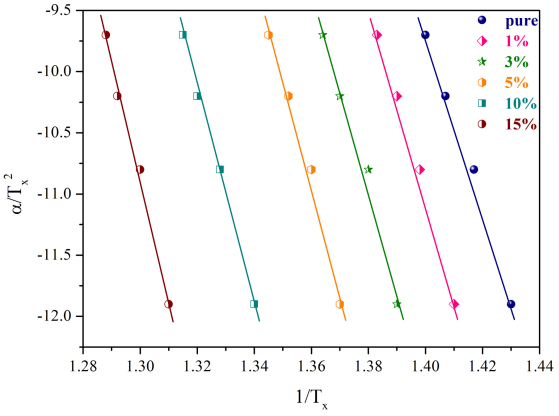

Fig. 2. Kissinger plots, the plot of (α/T_x^2) vs $1/T_x$ for crystal growth of the samples prepared for calculations of the E_a values.

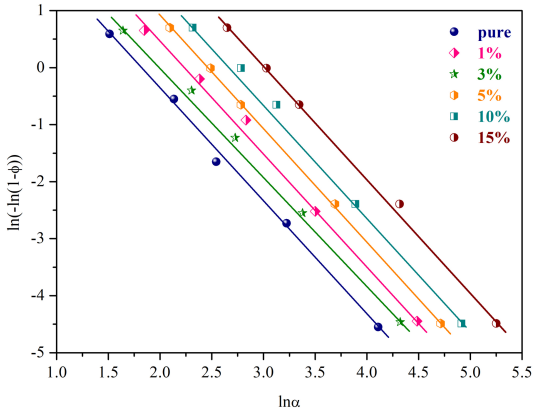

Fig. 3. Plots of $\ln(-\ln(1-\varphi))-\ln(\alpha)$ for computation of the parameter n in pure and MWCNT-added samples.

As is known in crystallization theory, crystal growth is generally based on the formation of two-dimensional surface nucleation. Here in this study, the calculated activation energy (E_a) represents the crystallization that occurs by ionic migration along the nucleus-melt interface, where the first crystallization begins around the nucleation centers. It is, therefore, important to obtain the initial crystallization temperature, which gives the first crystallization activation energy for glass–ceramic BSCCO, because at higher temperatures, crystal growth occurs in initiated crystals rather than initiation of crystallization.

The calculations of the crystallization kinetics of the prepared samples were made using the Kissinger model to understand if there is any change with the MWCNT addition. The Kissinger model is given as [29, 42, 43]

$$\frac{\mathrm{d}\left[\ln\left(\alpha/T_x^2\right)\right]}{\mathrm{d}\left(1/T_x\right)} = \frac{E_a}{R} + \text{constant}. \qquad (1)$$

In (1), T_x is the peak of the first crystallization temperature and is used for the calculation of E_a, α is the heating rate used in the experiment, R is the gas constant, and E_a is the activation energy for crystal growth. According to the model, if the form of crystallization does not change with the heating rate, E_a is then attained from the plot of (α/T_x^2) vs $1/T_x$ (see Fig. 2). Table I lists the calculated E_a values for MWCNT-added glass–ceramic samples. By taking into account the MWCNT addition and the heating ramp rate, the E_a values were found between 331 and 359 kJ/mol. Previously obtained results for BSCCO materials, including different substitution and/or doping levels by different research groups, showed that the value of E_a could be between 75 and 355 kJ/mol [44–46]. In this study, the E_a value was found between 331 and 359 kJ/mol, and it was determined that E_a slightly increased as the MWCNT addition increased.

This shows that adding even a small amount of MWCNT makes a contribution to the crystallization kinetics of the BSCCO system and suggests that this fast-cooled system, from higher viscosity, exhibits more stable nucleation and crystal growth. Moreover, $\Delta T = T_x - T_g$ was found broad enough to work even in higher MWCN additions. Furthermore, we calculated the Avrami parameter using the Ozawa equation to have detailed information on the crystal formation of the MWCN-added sample. The Ozawa equation is given as [47, 48]

$$\frac{\mathrm{d}\left[\ln\left(-\ln\left(1-\varphi\right)\right)\right]}{\mathrm{d}\left(\ln\alpha\right)} = -n. \qquad (2)$$

In (2), α is the heating rate, φ value is a temperature determined as the maximum points of the exothermic peaks of the first crystallization temperature obtained at different heating ramps, and n is the Avrami parameter. Accordingly, the slope of the straight line, obtained from the plot of $\ln(-\ln(1-\varphi))$ vs $\ln(\alpha)$, gives the n parameter.

Figure 3 shows the $\ln(-\ln(1-\varphi))$ vs the $\ln(\alpha)$ plot of the pure and MWCNT-added samples. According to information in the literature, the n value for diffusion-controlled growth in BSCCO glass–ceramics is expected to be $1.5 < n < 2.5$ [45, 49].

TABLE II

Crystallographic parameters, hole concentrations, and EDS result of carbon in the samples prepared. Error in EDS analysis is ±0.01.

MWCNT addition [wt%]	Crystal parameter		Crystalline size [Å]	Hole content p	EDS result for C [%]
	a [Å]	c [Å]			
0.0	5.402(5)	30.599(5)	232	0.201	0.0
1	5.402(5)	30.599(5)	233	0.205	> 1
3	5.402(6)	30.600(5)	234	0.213	2.6
5	5.403(5)	30.605(5)	247	0.221	4.7
10	5.405(6)	30.609(5)	255	0.235	9.6
15	5.406(5)	30.614(5)	264	0.247	13.9

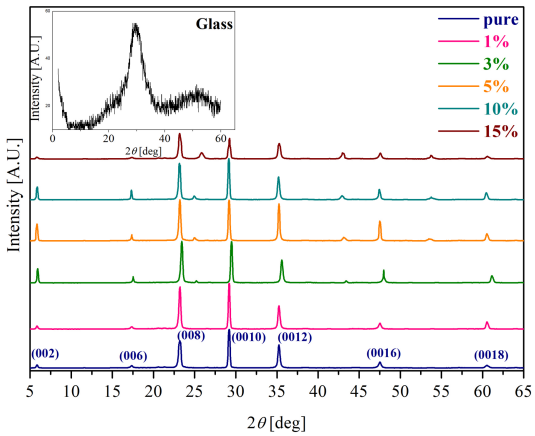

Fig. 4. XRD patterns of samples prepared. Insert show 5 wt% MWCNT-added Glass material just after melting.

In our case, the n value for the produced samples was found to be between 2.11 and 2.39 (Table I) and agrees with the values obtained for various BSCCO glass–ceramic samples prepared in previous studies done by different research groups [10–13, 50]. Moreover, the result presented in this work indicates that homogeneous nucleation is dominant in the matrix, and, accordingly, the growth of the crystal is diffusion-controlled, and most importantly, nucleation and crystal growth occurred simultaneously on the surface of the glass samples produced.

3.2. Structural analysis

The X-ray diffraction patterns of the samples prepared, including the BSCCO glass sample with 5 wt% MWCNT addition are shown in Fig. 4. As seen in the insert in Fig. 4, a halo — the general property of the glasses — was obtained at $2\theta \approx 30°$.

This clearly shows that there is no 3-dimensional arrangement in the matrix. For the crystalline material, no trace of carbon peaks was obtained up to the 5 wt% addition level. Also, no other impurity peaks, such as Al_2O_3 due to the crucible used during melting, were observed for all samples produced. However, starting from the addition level of 5 wt%, the carbon peaks began to appear at $2\theta = 25$, 43, and 53°, and their intensity increased with the addition. However, the absence of any impurity phases other than MWCNT, such as (SrCa)CuO or CuO, indicates that the produced glass–ceramic samples are single-phase $Bi_2Sr_2CaCu_2O_{8+s}$. Moreover, it is seen that samples produced have a uniform orientation along the c-axis, and it reaches its highest value at the addition level of 5 wt%, but for higher addition levels such as 10 and 15 wt%, orientation becomes weaker, the peak intensities started to decrease, and more flattened peak structure was obtained.

It was determined that the crystal symmetry of the produced samples was tetragonal. For the pure sample, the unit cell parameters were calculated as $a(= b) = 5.4022$ Å and $c = 30.5998$ Å. But as seen in Table II, in the MWCNT-added samples, the $a(= b)$-axis was almost remaining unaffected, while the c-axis increased slightly with the addition of MWCNT.

The appearance of carbon peaks as the MWCNT concentration increases suggests that a certain portion of MWCNTs remains unreacted in the BSCCO matrix. However, it is thought that some of them may react with Ca, Sr,or O atoms to form new phases. Phases formed in this way, at the atomic scale, cannot be detected by XRD and SEM, and detailed transmission electron microscopy analysis is required. However, it is thought that the limited binding ability of C with Ca, Sr, and O atoms may result in a distortion in the BSCCO structure, which may result in a change along the c-axis.

We calculated the crystalline size of samples using the Scherrer method [51], which is given as

$$\lambda S_c = \frac{0.98}{z\cos(\theta)}, \tag{3}$$

where S_c is crystalline size, λ the wavelengths of the X-ray used, θ the peak angle, and z is the broadening of the XRD peaks. Calculations according to (3) showed that the crystalline sizes increased from 232 to 264 Å with the MWCN addition rate (see Table II). This means that the addition of MWCNTs can change the thermodynamic properties of

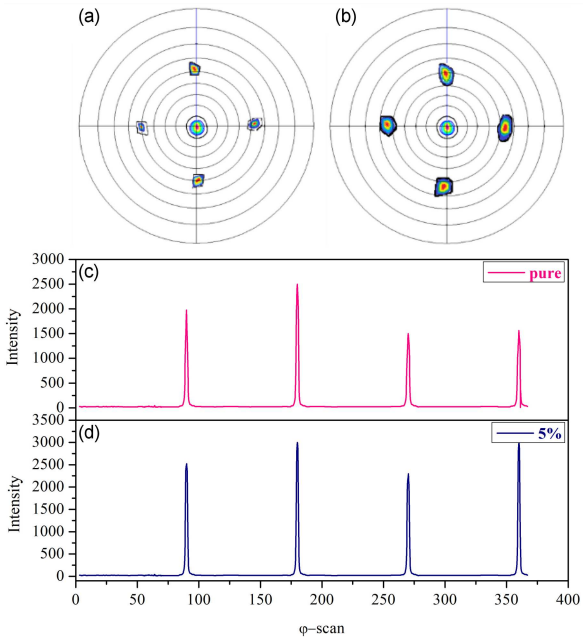

Fig. 5. (a) Pole position intensity of a) pure sample, (b) 5 wt% MWCNT-added sample as an example, (c) φ-scan curves of (0010) reflection lines of pure sample, and (d) φ-scan curves of (0010) reflection lines of 5 wt% MWCNT-added glass–ceramic sample.

the structure and therefore has a positive effect on crystal growth. Thus slightly larger crystals were formed by the addition of MWCNTs.

We also determined the grain alignment of the samples using X-ray pole figure data and φ-scan curves of (0010) reflection lines. Figure 5a and b shows the pole position intensities of pure and 5 wt% MWCNT-added samples, respectively, and Fig. 5c and d shows φ-angles of the same samples as an example. For both samples, four symmetrically distributed poles around the center, which is characteristic of tetragonal symmetry, have been obtained.

However, it was found that the pole density was more pronounced in the 5 wt% MWCNT-added sample than in the pure and/or other MWCNT-added samples. At the addition of 10 wt%, it was found that the pole density started to be distributed randomly rather than in a regular way, and the orientation was weakened accordingly. In the 15 wt% MWCNT-added sample the pole density almost disappeared. This indicates that the 5 wt% MWCNT-added sample is highly textured, the c-axis is largely perpendicular to the sample surface, and therefore grain disorientations are very low.

The analysis of φ-scan showed that the intensity of the peaks of the 5 wt% MWCNT-added sample was slightly higher than that of the other samples. The full width at half maximum (FWHM) value is 2.82 for 5 wt% MWCNT-added and 3.14 for the pure sample. FWHMs of other samples were found to vary between 3.57 and 5.19, which clearly shows

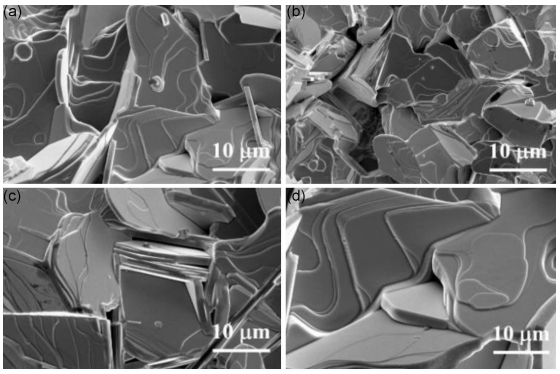

Fig. 6. SEM images of (a) pure sample and (b) 1 wt% MWCNT-added, (c) 5 wt% MWCNT-added and (d) 15 wt% MWCNT-added samples.

that the 5 wt% MWCNT-added sample has a good in-plane alignment. This confirms the patterns obtained from XRD results in Fig. 4.

3.3. Microstructural analysis

In Fig. 6a–d, SEM images of the pure and with 5, 10, and 15 wt% MWCNT addition samples are given as an example; a similar morphology was obtained in other samples. In general, the surface morphologies represent the classical BSCCO structure, and it was observed that there was no significant change with MWCNT addition. Also, no impurities and/or agglomerated MWCNT were observed on the surface. This showed that MWCNTs are embedded in the main BSCCO matrix and incorporated with the BSCCO material. However, a transmission electron microscopy (TEM) study would be essential to properly elucidate this issue.

The results of the EDS analyses of the samples for MWCNT are given in Table II. In the analyses made on the surface of the samples, after the surface roughness was removed and polished, it was observed that the carbon ratio in the matrix increased as the MWCNT addition increased. This confirms the result of the XRD analysis. In addition, analyses performed at different locations for each sample yield similar results, indicating that MWCNT is homogeneously dispersed in the matrix. In addition, about 1.1% of Al_2O_3 contamination was obtained in the samples due to the Al_2O_3 crucible in the melting stage. However, this may be desirable because it is well known that the Al_2O_3 supports glass formation. These results remain within the error limit ($\sim$ 2%) of the EDS system.

3.4. Resistivity analysis

Figure 7a–f shows the resistivity measurement result of samples pure and with 1, 3, 5, 10, and 15 wt% MWCNT addition between 0 and 8 T applied fields. The T_c and T_{zero} values were increasing up to 5 wt% of MWCNT addition in the sample, and a maximum result was obtained, but then started to

TABLE III

Electrical and magnetic properties of glass–ceramic samples prepared at zero field. Error in measurements is < 0.02.

MWCNT addition level [wt%]	T_{onset} [K]	T_{zero} [K]	ΔT [K]	J_c^{mag} [A/cm^2] at 4.2 K	J_c^{trans} [A/cm^2] at 4.2 K
0.0	93.6	90.0	3.6	2.1×10^6	1.9×10^6
1	94.0	91.5	2.5	3.0×10^6	2.0×10^6
3	94.2	92.1	2.1	3.8×10^6	2.1×10^6
5	94.4	92.8	1.6	4.1×10^6	2.3×10^6
10	92.7	89.9	2.8	0.9×10^6	1.7×10^6
15	91.9	87.8	4.1	0.2×10^6	1.09×10^6

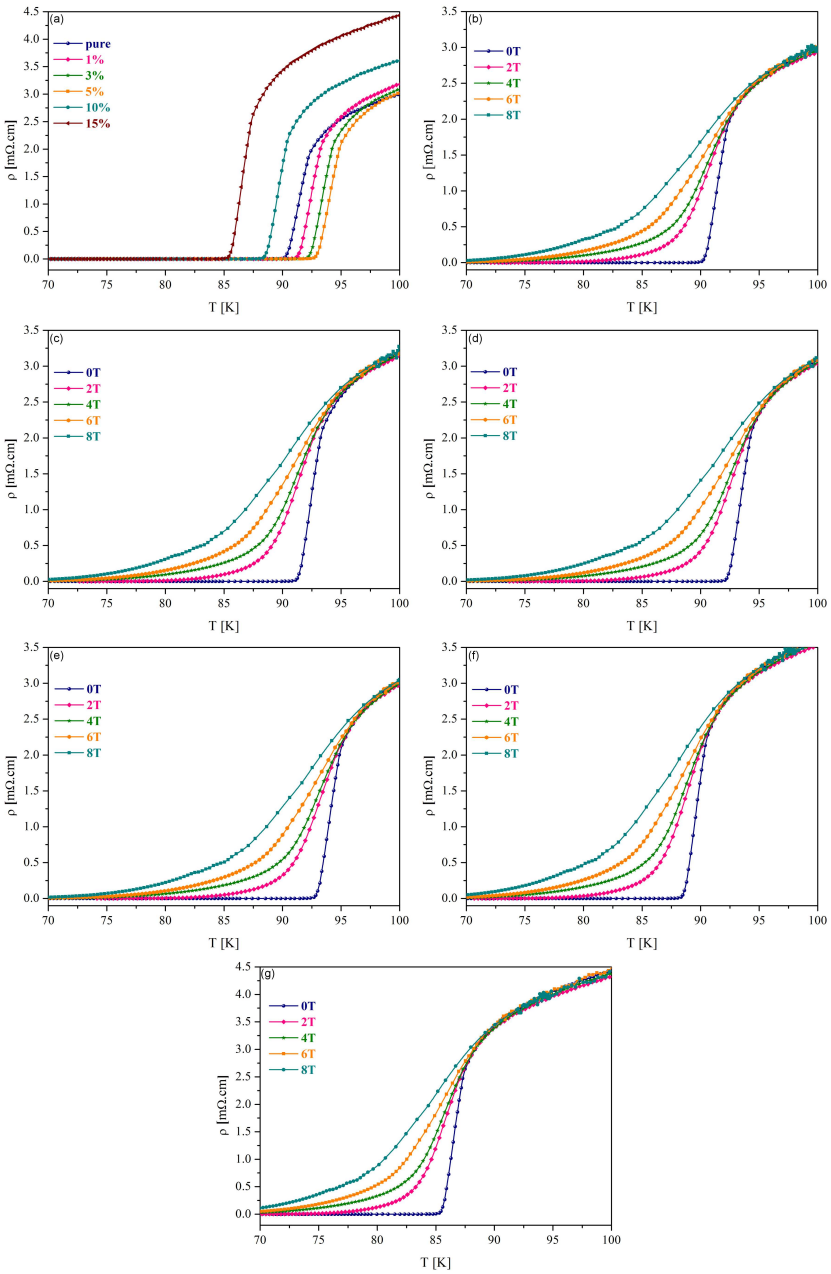

Fig. 7. Resistivity measurement result of (a) all samples at zero field, (b) pure sample, (c) 1 wt% MWCNT-added, (d) 3 wt% MWCNT-added, (e) 5 wt% MWCNT-added, (f) 10 wt% MWCNT-added and (g) 15 wt% MWCNT-added samples up to 8 T applied fields.

decrease with the 10 and 15 wt% MWCNT addition. The best result obtained was 94.4 and 92.8 for, respectively, T_c and T_{zero} for the 5 wt% MWCNT-added sample. However, with additions above 5 wt%, normal state resistance also started to increase (by approximately 5%), and the T_{zero} value decreased significantly. This situation can be seen clearly in the values ΔT ($\Delta T = T_{\text{onset}} - T_{\text{zero}}$) given in Table III. It is thought that this situation is probably due to the fact that the conduction paths are significantly affected as a result of the dislocations that occur due to the chemical interactions as the MWCN ratio increases in the matrix.

In order to understand this situation more clearly, we tried to calculate the hole numbers in the CuO planes for all samples. To calculate the hole number p, we used

$$\frac{T_c}{T_c^{\max}} = 1 - 82.6\,(p - 0.16)^2\,, \qquad (4)$$

where $T_c^{\max}$ is taken as 90 K, which is a generally accepted value for the $Bi_2Sr_2CaCu_2O_x$ material, and p is the number of holes for each Cu [52]. As a result of the calculations, it has been seen that the p values were between 0.201 and 0.247 and increased as the MWCNT addition was increased (see Table II). It was previously calculated that the mean p-value for the BSCCO system was between 0.16 and 0.116 for $Bi_2Sr_2Ca_2Cu_3O_y$, between 0.22 and 0.16 for $Bi_2Sr_2CaCu_2O_x$, and higher than 0.22 for $Bi_2Sr_2Cu_1O_y$ [6, 50, 53, 54]. In this work, for the low MWCNT additions, such as the 1, 3, and 5 wt% addition cases, the p-value was found to be close to the upper limit of the $Bi_2Sr_2CaCu_2O_x$ system, but as the addition rate increases, the upper limit of 0.22 is exceeded. Obviously, p is well known to vary with oxygen content in the structure during the annealing stage and also with substitutions and/or additives. It is also known that p varies with the formation of stacking faults, particularly during the melting stage, where C atoms dissolve to produce new atomic-sized impurity phases with Ca, Sr, or oxygen [55]. It is considered that these atomic phases may remain as staking faults, possibly in Cu–O layers within the BSCCO structure. Thus this kind of formation plays an important role in the change of p and may occur from an optimally doped region to an over-doped state. This suggests a shift of the hole concentration range from the optimally doped region for $Bi_2Sr_2CaCu_2O_x$ to the over-doped region of $Bi_2Sr_2Cu_1O_y$. As a result, for high addition cases, such as the 10 and 15 wt% MWCNT levels, high hole concentration can be possible in Cu–O planes, and therefore superconductivity partly deteriorates.

3.5. *I–V* measurement analysis

In Fig. 8a, the transport *I–V* graph of all samples prepared, taken at zero fields, and in Fig. 8b, of the 5 wt% MWCNT-added sample, which gives the best result, examined between 0 and 8 T, are given. It was found that as MWCNT addition was increased, J_c^{trans} increased and reached the best value in the

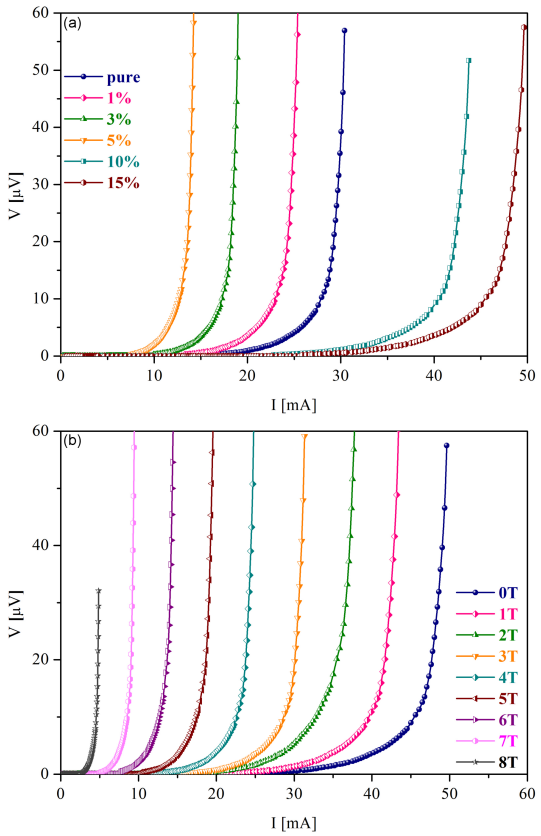

Fig. 8. (a) Transport *I–V* graph of all samples prepared, taken at zero fields, and (b) *I–V* graph of 5% MWCNT added sample, as an example.

5 wt% added sample (see Fig. 8a). However, when the addition increased further, the J_c^{trans} value decreased significantly (see Table III). Under the magnetic field, the *I–V* properties exhibited a behavior very similar to the classical undoped BSCCO system. The J_c^{trans} value systematically decreased as the applied magnetic field increased but did not drop completely to zero even at 8 T, as shown in Fig. 8b for the 5 wt% MWCNT-added sample.

This situation is actually similar to the results obtained in the resistivity–temperature measurements. It is thought that this can be explained by the damage in the conduction paths due to the chemical pressure that formed as a result of the increase in MWCNT concentration and also the occurrence of some atomic-sized disturbances, probably the emergence of new non-conductive phases as a result of the reaction with MWCNT and BSCCO material at high temperatures within in the matrix.

3.6. *M–H* measurement analysis

M–H measurement of samples was taken between ±8 T, and results obtained for the pure, 5, 10, and 15% MWCNT-added samples are given in Fig. 9, as an example. It was observed that the magnetization trends of the samples were similar and that there was no large difference in the shape of the hysteresis

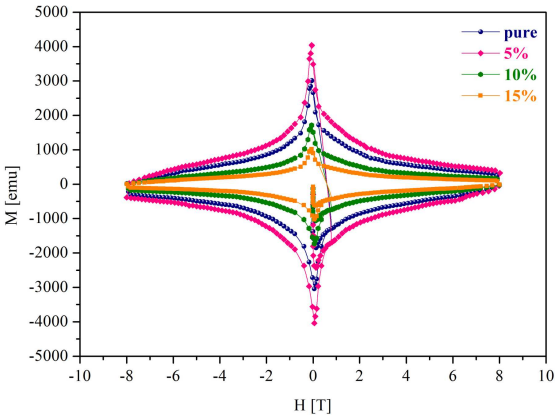

Fig. 9. The M–H curves of pure, 5 wt% MWCNT-added, 10 wt% MWCNT-added, and 15 wt% MWCNT-added samples between ±8 T applied fields.

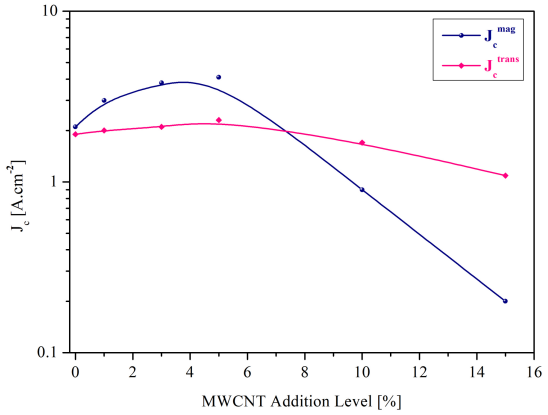

Fig. 10. Results of J_c^{mag} and J_c^{trans} measurement vs MWCNT addition of the samples produced.

due to MWCNT addition, which indicates typical granular HTS materials. However, the magnitude of the magnetization increased by approximately 20% in the 5 wt% MWCNT-added sample compared to the pure one. However, a gradual decrease was observed for the 10 and 15 wt% MWCNT-added samples. For the calculation of the magnetization critical current density (J_c^{mag}), we used the M–H curves and the Bean formulation. Bean formulae for the rectangular sample can be given as [55, 56]

$$J_c^{\mathrm{mag}} = \frac{20\,\Delta M}{a\left(1-\frac{a}{3b}\right)}. \qquad (5)$$

In (5), J_c^{mag} gives the critical current density in ampere per square centimeter [A/cm^2], and $\Delta M = M^+ - M^-$ is the difference in magnetization in electromagnetic units per cubic centimeter [emu/cm^3], calculated from the positive and negative magnetization difference in the M–H curves. In (5), a and b ($a < b$) are the cross-sectional size of samples in centimeters. Calculated J_c^{mag} values for all samples at 4.2 K are given in Fig. 10 and Table III. To minimize the error during analysis, we ran 3 different measurements consecutively in the same series of samples, and the average value was then taken into account. The maximum value for $J_c^{\mathrm{mag}} = 4.1 \times 10^6$ A/cm^2 was calculated for the 5 wt% MWCNT-added sample as in the J_c^{trans} measurements. It shows an increase of about 45% compared to the pure sample. However, after a 5 wt% addition, the J_c^{mag} value decreased dramatically due to decreased magnetization in the M–H curves.

As a result, it was seen that even a small amount of MWCNTs addition to the BSCCO material increased J_c^{mag} compared to the pure sample. It has been evaluated that small-sized MWCNTs form non-superconducting phases in the BSCCO matrix, possibly in a point form, during heat treatment in an oxygen atmosphere at high temperatures, and they act as pinning centers up to a certain concentration of doping, and accordingly, the J_c value increases. When the additive concentration increases further, it is considered that these pinning centers probably expand excessively and begin to lose their trapping feature, and also, they take on the impurity phase format, as seen in the XRD analyses, and produce fractional barriers for superconducting current, and then start to have an adverse effect on J_c.

4. Conclusions

In this study, the 0, 1, 3, 5, 10, and 15 wt% MWCNT-added $Bi_2Sr_2CaCu_2O_{8+s}$ glass–ceramic superconductors were prepared. Thermal, physical, electrical, and magnetic properties were characterized. It was found that the E_a values slightly increased by increasing the addition level. Also, based on the DTA data, the Avrami parameter n was calculated and found to be between 2.11 and 2.39. This indicates that homogeneous nucleation is dominant in the matrix, and accordingly, the growth of the crystal is diffusion-controlled, and most importantly, nucleation and crystal growth occurred on the surface of the glass samples. XRD analyses showed that all samples have tetragonal symmetry and did not change with MWCNT addition, but a small change in the c-axis is observed, which appears to cause an expansion in the cell volume of the BSCCO structure.

Moreover, according to SEM analyses, no significant morphological change was obtained with the addition.

The effect of MWCNT addition on the resistivity measurements was limited, and only a 2.8 K increase in the T_{zero} value was obtained for the best sample. The hole concentration value of the samples was also calculated, and it was established that there was a shift towards the over-doped region with the increase in MWCNT concentration, which suppressed the superconductivity in samples with high MWCNT addition. The best J_c^{trans} and J_c^{mag} results were obtained in the 5 wt% MWCNT-added sample. However, they decrease gradually in high-addition cases. Consequently, at the beginning of

this study, we expected that MWCNTs could form pinning centers in the structure due to their very small cylindrical structure. However, it has been seen that this situation can be possible in the case of non-superconducting cylindrical small dots by reacting with the oxygen or other atomic-scale impurities in the BSCCO matrix during the heat treatment at high temperatures up to a certain MWCNT concentration. However, it is believed that pinpoint high-resolution TEM imaging is required to confirm this claim.

Acknowledgments

K. Yakinci and Ö. Çiçek thank Prof. Dr. M.E. Yakinci for allowing us to use his experimental setup and for his valuable comments on the results obtained.

References

[1] H. Maeda, Y. Tanaka, M. Fukutomi, T. Asano, *Jpn. J. Appl. Phys.* **27**, L209 (1988).

[2] M.S. Shalaby, H.M. Hashem, T.R. Hammad, L.A. Wahab, K.H. Marzouk, S. Soltan, *J. Radiat. Res. Appl. Sci.* **9**, 345 (2016).

[3] A.I. Golovashkin, O.M. Ivanenko, Yu.B. Kudasov, K.V. Mitsen, A.I. Pavlovsky, V.V. Platonov, O.M. Tatsenko, *Physica C: Supercond.* **185–189**, 1859 (1991).

[4] F.M. Costa, N.M. Ferreira, S. Rasekh, A.J.S. Fernandes, M.A. Torres, M.A. Madre, J.C. Diez, A. Sotelo, *Cryst. Growth Des.* **15**, 2094 (2015).

[5] M. Giura, R. Fastampa, S. Sarti, E. Silva, *Phys. Rev. B* **68**, 134505 (2003).

[6] A. Sedky, A. Salah, A.A. Bahgat, A. Abou-Aly, *J. Mater. Sci. Mater. Electron.* **31**, 12502 (2020).

[7] N.K. Saritekin, M. Pakdil, E. Bekiroglu, G. Yildirim, *J. Alloys Compd.* **688**, 637 (2016).

[8] V.N. Zavaritsky, *Physica C: Supercond.* **235-340**, 2715 (1994).

[9] Y. Yamada, T. Watanabe, M. Suzuki, *IEEE Trans. Appl. Supercond.* **17**, 3533 (2007).

[10] M.A. Aksan, M.E. Yakinci, *J. Alloys Compd.* **385**, 1 (2004).

[11] M. Ozabaci, M.A. Aksan, G. Kirat, O. Kizilaslan, M.E. Yakinci, *J. Non-Cryst. Solids* **454**, 8 (2016).

[12] M.A. Aksan, M. E. Yakinci, K. Kadowaki, *J. Supercond. Nov. Magn.* **23**, 371 (2010).

[13] W. Zhang, E.E. Hellstrom, *Physica C: Supercond.* **218**, 141 (1993).

[14] S. Altin, M. A. Aksan, Y. Balci, M.E. Yakinci, *J. Supercond. Nov. Magn.* **22**, 775 (2009).

[15] P. Agarwala, M.P. Srivastava, P.N. Dheer, V.P.N. Padmanaban, A.K. Gupta, *Physica C: Supercond.* **313**, 87 (1999).

[16] X. Zhao, W. Liu, T. Wang, A. Liu, T. Li, Y. Chen, X. Liu, X. Ma, B. Sun, Y. Qi, *Colloids Surf. A: Physicochem. Eng. Aspects* **627**, 127121 (2021).

[17] T. Terai, T. Kobayashi, K. Kishio, J. Shimoyama, S. Okayasu, Y. Kazumata, *Physica C: Supercond. Appl.* **282**, 2135 (1997).

[18] H. Fallah-Arani, S. Baghshahi, A. Sedghi, N. Riahi-Noori, *Ceram. Int.* **45**, 21878 (2019).

[19] T. Komatsu, M. Ueta, T. Ohki, R. Sato, K. Matusita, *J. Am. Ceram. Soc.* **25**, 1864 (1992).

[20] Y. Abe, H. Arakawa, M. Hosoe, Y. Hikichi, J. Iwase, H. Hosono, Y. Kubo, *Jpn. J. Appl. Phys.* **28**, L1929 (1989).

[21] Y. Higashida, H. Yokoyama, K. Michishita, Y. Kubo, H. Yoshida, *Appl. Phys. Lett.* **55**, 1578 (1989).

[22] T. Komatsu, R. Sato, K. Matusita, *Appl. Phys. Lett.* **54**, 1169 (1989).

[23] J.Y. Oh, D.S. Yang, D.H. Tran, B. Kang, *Ceram. Int.* **46**, 8259 (2020).

[24] M.S. Shalaby, Mai Hussein Hamed, N.M. Yousif, H.M. Hashem, *Ceram. Int.* **47**, 25236 (2021).

[25] D.T. Tran, A.T. Pham, H.H. Pham, N.T. Nguyen, N.H. Nam, N.K. Man, W.-N. Kang, I-J. Hsu, W. Klysubun, D.T. Tran, *Ceram. Int.* **47**, 16950 (2021).

[26] R. Sato, T. Komatsu, K. Matusita, *J. Mater. Sci. Lett.* **10**, 355 (1991).

[27] A. Harabor, P. Rotaru, N.A. Harabor, *Ceram. Int.* **45**, 2742 (2019).

[28] P.M. Sarun, S. Vinu, R. Shabna, A. Biju, P. Guruswamy, U. Syamaprasad, *IEEE Trans. Appl. Supercond.* **19**, 35 (2009).

[29] E. Altin, D. M. Gokhfeld, S. Demirel, E. Oz, F. Kurt, S. Altin, M. E. Yakinci, *J. Mater. Sci. Mater. Electron.* **25**, 1466 (2014).

[30] X. Sun, X.Zhao, W. Wu, X. Fan, X.-G. Li, H.C. Ku, *Physica C: Supercond.* **307**, 67 (1998).

[31] Q. Li, H.B. Pan, C.G. Zhu, P.S. Xu, X.Y. Zhang, *J. Supercond.* **13**, 565 (2000).

[32] P. Murugakoothan, R. Jayavel, C.R. Venkateswara Rao, C. Subramanian, P. Ramasamy, *Supercond. Sci. Technol.* **7**, 367 (1994).

[33] S.Y. Li, Q. Cao, Z. Sun, X.H. Chen, L.Z. Cao, *Supercond. Sci. Technol.* **13**, 1595 (2000).

[34] B. Chattopadhyay, B. Bandyopadhyay, A. Poddar, P. Mandal, A.N. Das, B. Ghosh, *Physica C: Supercond.* **331**, 38 (2000).

[35] R.K Nkum, *J. Mater. Sci.* **33**, 207 (1998).

[36] H.L. Liu, D.B. Tanner, H. Berger, G. Margaritondo, *Physica C: Supercond.* **311**, 197 (1999).

[37] D.H. Galvan, A. Durán, F. F. Castillón, E. Adem, R. Escudero, D. Ferrer, A. Torres, M. José-Yacamán, *J. Supercond. Nov. Magn.* **21**, 271 (2008).

[38] K. Fossheim, E.D. Tuset, T.W. Ebbesen, M.M.J. Treacy, Justin Schwartz, *Physica C: Supercond.* **248**, 195 (1995).

[39] D.H. Galván, JunHo Kim, M.B. Maple, G.A. Hirata, E. Adem, *Physica C: Supercond.* **341–348**, 1269 (2000).

[40] S.-L. Huang, M.R. Koblischka, K. Fossheim, T.W. Ebbesen, T.H. Johansen, *Physica C: Supercond. Appl.* **282–287**, 2279 (1997).

[41] D.H. Galvan, Shi Li, W.M. Yuhasz, J.H. Kim, M.B. Maple, E. Adem, *Physica C: Supercond.* **403**, 145 (2004).

[42] K. Matusita, S. Sakka, *J. Non-Cryst. Solids* **38–39**, 741 (1980).

[43] W.A Johnson, R.F. Mehl, *Trans. Am. Inst. Electr. Eng.* **135**, 416 (1939).

[44] N.P. Bansal, *J. Appl. Phys.* **68**, 1143 (1990).

[45] A. Karamanov, M. Pelino, *J. Non-Cryst. Solids* **290**, 173 (2001).

[46] J. Danusantoso, T.K. Chaki, *Supercond. Sci. Technol.* **4**, 509 (1991).

[47] T. Ozawa, *Polymer* **12**, 150 (1971).

[48] T.L. Shanker Rao, K.N. Lad, A. Pratap, *J. Therm. Anal. Calorim.* **78**, 769 (2004).

[49] Z.J. Yan, S.R He, J.R Li, Y.H Zhou, *J. Alloys Compd.* **368**, 175 (2004).

[50] M.A. Aksan, M.E. Yakinci, *J. Mater. Process. Technol.* **196**, 365 (2008).

[51] B.D. Cullity, *Elements of X-Ray diffraction* Addision-Wesley, San Diego (CA) 1978, p. 281.

[52] M.R. Presland, J.L. Tallon, R.G. Buckley, R.S. Liu, N.E. Flower, *Physica C: Supercond.* **176**, 95 (1991).

[53] G. Akça, A. Ekicibil, K. Kıymaç, *J. Optoelectron. Adv. Mater.* **15**, 229 (2013).

[54] F. Kahraman, A. Sotelo, M.A. Madre, J.C. Diez, B. Ozkurt, Sh. Rasekh, *Ceram. Int.* **41**, 14924 (2015).

[55] P.G. De Gennes, *Superconductivity of Metals and Alloys*, Westview press, Los Angeles 1966.

[56] C.P. Bean, *Phys. Rev. Lett.* **8**, 250 (1962).